RESEARCH ARTICLE

Correspondence to:
R. He,
rhe@ncsu.edu

Variational data assimilative modeling of the Gulf of Maine in spring and summer 2010

Yizhen Li[1,2], Ruoying He[1], Ke Chen[3], and Dennis J. McGillicuddy[2]

[1]Department of Marine, Earth, and Atmospheric Sciences, North Carolina State University, Raleigh, North Carolina, USA, [2]Department of Applied Ocean Physics and Engineering, Woods Hole Oceanographic Institution, Woods Hole, Massachusetts, USA, [3]Department of Physical Oceanography, Woods Hole Oceanographic Institution, Woods Hole, Massachusetts, USA

Abstract A data assimilative ocean circulation model is used to hindcast the Gulf of Maine [GOM] circulation in spring and summer 2010. Using the recently developed incremental strong constraint 4D Variational data assimilation algorithm, the model assimilates satellite sea surface temperature and in situ temperature and salinity profiles measured by expendable bathythermograph, Argo floats, and shipboard CTD casts. Validation against independent observations shows that the model skill is significantly improved after data assimilation. The data-assimilative model hindcast reproduces the temporal and spatial evolution of the ocean state, showing that a sea level depression southwest of the Scotian Shelf played a critical role in shaping the gulf-wide circulation. Heat budget analysis further demonstrates that both advection and surface heat flux contribute to temperature variability. The estimated time scale for coastal water to travel from the Scotian Shelf to the Jordan Basin is around 60 days, which is consistent with previous estimates based on in situ observations. Our study highlights the importance of resolving upstream and offshore forcing conditions in predicting the coastal circulation in the GOM.

1. Introduction

The Gulf of Maine [GOM] encompasses a coastal area of northeastern North America between Nova Scotia in the northeast and Cape Cod in the southwest [Figure 1]. The region is dominated by a cyclonic circulation [e.g., *Bigelow*, 1927; *Beardsley et al.*, 1997] that is influenced by both local forcing such as wind, heat flux, river discharge [*Brown and Irish*, 1992; *Brooks*, 1994; *Keafer et al.*, 2005], tidal rectification [*Lynch et al.*, 1996, 1997] and upstream and deep-ocean forcing [*Smith*,1983; *Smith et al.*, 200l, 2012]. Cold and fresh Scotian Shelf Waters (SSW) enter the gulf from the northeast with an annual mean transport of ∼0.14 Sv [e.g., *Chapman and Beardsley*, 1989; *Smith*, 1983], and warm slope waters can enter the GOM through the Northeast Channel [e.g., *Townsend et al.*, 2010; *Pettigrew et al.*, 2011].

Numerical modeling has long been used to advance the understanding of the GOM circulation dynamics and variability. Earlier modeling studies have focused on various aspects of GOM circulation, such as climatological mean states [*Lynch et al.*, 1997; *Xue et al.*, 2000], or synoptic to seasonal scale hindcasts [*Hetland and Signell*, 2005; *He and McGillicuddy et al.*, 2008; *Li et al.*, 2009]. In these studies, ocean models were solved as initial and boundary-value problems (so called "forward" model), and additional observations were used only for model validation.

A few inverse modeling studies used coastal sea level and velocity observations in the GOM and interior regional seas [*Signell et al.* 1994; *Lynch et al.*, 1998; *Lynch and Hannah*, 2001; *He et al.*, 2005; *Aretxabaleta et al.*, 2009] to refine model open boundary conditions, which in turn help to improve predictive skill. In these examples, both surface forcing and model initial conditions were known and assumed to be error free; the open boundary condition was refined using local observations. Recent advancements in 4-dimensional variational data assimilation (4D-Var) techniques [*Powell et al.*, 2008; *Broquet et al.*, 2009a, 2009b; *Moore et al.*, 2011a, *Arango et al.*, 2011; *Matthews et al.*, 2012; *Chen et al.*, 2014] provide a major step forward. They allow observations to be used to constrain models by refining boundary conditions, initial conditions, and surface forcing, and therefore hold a great promise in realistically simulating coastal ocean state variables.
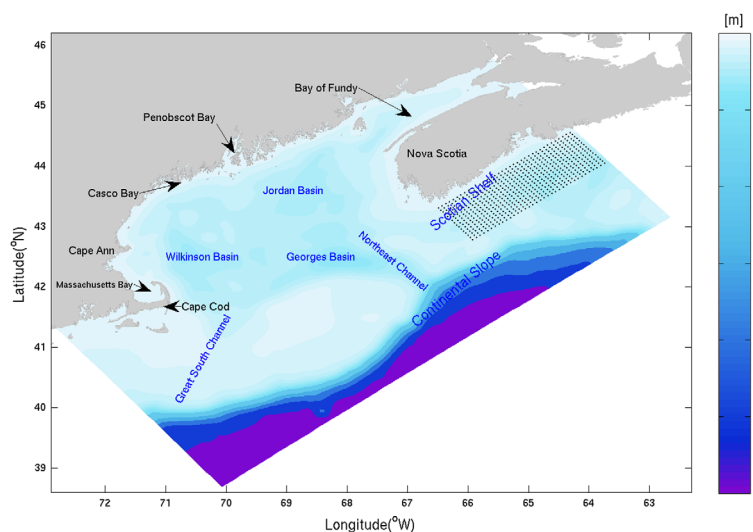
Figure 1. Model bathymetry for the Gulf of Maine (GOM) 5 km model. Black dashed lines represent the 200 m isobath. Important geographic locations are also labeled, including the Bay of Fundy (BOF), and Northeast Channel (NEC). Black dots indicate the initial locations for particle release to quantify the time scale for transport from the Scotian Shelf to Jordan Basin.

In summer 2010, anomalous hydrographic conditions were noted in the Gulf of Maine. Observational evidence suggested more Scotian Shelf Water (SSW) and Slope Sea waters entered the gulf [*McGillicuddy et al.*, 2011]. Changes in gulf-wide hydrography were accompanied by a weakened coastal flow in the western GOM, especially in the month of June [*Li et al.*, 2014a]. Modeling coastal circulation during this particular time period using the forward regional ocean model is very challenging because of deficiencies in the initial conditions, boundary conditions, and surface forcing of the model. Herein we utilize local observations, gulf-wide ship surveys, and satellite data in the 4D-Varframework to perform a data assimilative (DA) model hindcast for spring and summer 2010. The skill of DA hindcast in reproducing the anomalous water mass and coastal circulation is evaluated by comparing independent observations that are not assimilated. The processes that lead to the anomalous water mass and circulation are then diagnosed and quantified.

The remainder of the paper is organized as follows. Section 2 introduces our regional forward model, DA system and observations being used. Section 3 presents DA hindcast results and its comparisons with independent observations. In-depth discussions of coastal circulation dynamics and hydrographic evolution in spring and summer 2010 are given in section 4, followed by a summary in section 5.

2. Data and Methods

2.1. Model Configuration

The GOM circulation hindcast was performed using the Regional Ocean Modeling System (ROMS) [*Haidvogel et al.*, 2008; *Shchepetkin and McWilliams*, 2005]. ROMS employs split-explicit separation of fast barotropic and slow baroclinic modes, and is formulated in vertically stretched terrain-following coordinates. Details of the GOM ROMS setup are given in *He et al.* [2008]. Briefly, for the hydrodynamic open boundary conditions (OBCs), a multinested configuration was implemented to downscale global data assimilative Hybrid Coordinate Ocean Model (HYCOM/NCODA, http://hycom.rsmas.miami.edu/dataserver) solutions to a shelf-scale ROMS model [*Chen et al.*, 2014; *Chen and He*, 2014] and subsequently to the GOM ROMS model via a one-way nesting approach. The shelf-scale ROMS has a spatial resolution of 10 km (5 km) in the alongshore (cross-shelf) direction, and 36 vertical levels that have higher resolution near the surface and bottom to better resolve boundary layers. The method of *Marchesiello et al.* [2001] was applied to prescribe boundary values of tracers and baroclinic velocity. For the free surface and depth-averaged velocity boundary conditions, the method of *Flather* [1976] was used with the external values provided by HYCOM. The *Mellor and Yamada* [1982] closure scheme and the quadratic drag formulation were applied to compute the vertical turbulent mixing and the bottom friction specification, respectively.

The GOM ROMS has a spatial resolution of 6 km (4 km) in the alongshore (cross-shelf) direction, and 36 vertical levels. Because the current implementations of ROMS 4D-Var tangent-linear and adjoint models do not allow for radiation boundary conditions, clamped boundary conditions (for 3D momentum and tracers) were used with values defined by the shelf-wide ROMS model. We employed a 6-grid point sponge layer

(using viscosity values at the boundary that were five times higher than values in the model interior) at all three open boundaries to alleviate any spurious wave reflections produced by the clamped conditions. Within the sponge layers, nudging was applied to relax temperature, salinity to the shelf-scale ROMS solutions over a time scale of 4 days. Along the open boundaries, we also superimposed M_2 tidal sea level and depth-averaged velocity fluctuations using harmonics derived from an ADCIRC simulation of the western Atlantic [*Luettich et al.*, 1992].

Surface atmospheric forcing, including cloud fraction, precipitation, surface pressure and humidity, air temperature, surface wind, and shortwave radiation were obtained from the National Center for Environmental Prediction (NCEP), North America Regional Reanalysis (NARR). Spatial and temporal resolution of these forcing fields are 32 km and 3 h, respectively. They were applied in the standard bulk flux formulation [*Fairall et al.*, 1996, 2003] to derive wind stress and net surface heat flux. To further constrain the net surface heat flux, we followed the same approach used in *He and Weisberg* [2003] to relax the modeled SST field to NOAA Coast Watch daily, $1/10°$ cloud-free SST product with a time scale of 3 days. Fresh water runoff from five major rivers was also prescribed. These include the U.S. portion of the St Johns River, the Penobscot River, the Kennebec River, the Androscoggin River, and the Merrimack River. For each of them, United State Geological Survey (USGS) real-time river runoff measurement was used to specify freshwater volume transport.

The hindcast experiment focused on a three and a half month period from 1 April to 18 July 2010. The non-data assimilative forward model simulation was run for six and half years from 1 February 2004 to 1 August 2010 to provide the background state for the DA experiment. The GOM forward solutions were compared against coastal sea level observations, as well as moored T/S profiles and velocity measurements. The low frequency circulation variability was generally well captured by the model, as demonstrated by earlier studies [e.g., *He et al.*, 2008; *Li et al.*, 2009; *Li et al.*, 2014b]. However, the anomalous hydrographic conditions in 2010 [*McGillicuddy et al.*, 2011] were not well simulated by the HYCOM model, nor by subsequent shelf-scale ROMS and GOM ROMS simulations—thus the need for DA.

2.2. 4D Variational Data Assimilation System

The ROMS 4D-Var system includes the nonlinear forward model (NLROMS), the tangent linear model (TLROMS) and its adjoint model (ADROMS). The system provides tools for conducting various types of model prediction and analysis [*Moore et al.*, 2004; *Di Lorenzo et al.*, 2007; *Powell et al.*, 2008; *Broquet et al.*, 2009a, 2009b; *Moore et al.*, 2011b; *Chen et al.*, 2014]. The ROMS incremental strong constraint 4D-Var method is based on the incremental formulation described by *Weaver et al.* [2003]. A brief overview of this method is given below to aid discussions in later sections. More details on its implementation in ROMS can be found in *Powell et al.* [2008] and *Moore et al.* [2011a].

The ROMS prognostic variables are composed of: sea surface displacement η, potential temperature T, salinity S, and horizontal velocity (u, v). When the primitive equations are discretized and arranged on the ROMS grid, the individual grid point values at time t_i define the components of a state vector $x(t_i) = (T, S, \eta, u, v)^T$, where superscript T denotes vector transpose. The state vector is propagated forward in time by the discretized nonlinear model, subject to surface forcing conditions $f(t_i)$ for momentum, heat and freshwater fluxes, and lateral open boundary conditions $b(t_i)$. The state vector evolves according to

$$x(ti) = M(ti, ti-1)(x(ti-1), f(ti), b(ti)) \tag{1}$$

where $M(ti, ti-1)$ represents NLROMS acting on $x(ti-1)$, subject to forcing $f(ti)$ and boundary conditions $b(ti)$ during the time interval $[ti, ti-1]$.

The goal of 4D-Var is to compute the best estimate of the model state, also referred to as the analysis or posterior, namely $x^a(t)$. It minimizes, in a least-squares sense, the difference between the model and the observations. The solution $x(t_i)$ of NLROMS depends upon the choice of initial condition $x(t_0)$, boundary conditions $b(t)$ and surface forcing $f(t)$, all of which are subject to errors and uncertainties. As such, $x(t_0)$, $b(t)$ and $f(t)$ are referred to as control variables, and the problem of 4D-Var is reduced to identifying the appropriate combination of adjustments to control variables that yield the best estimate $x^a(t)$.

According to *Courtier* [1997], the control variable increment is introduced as

$$\delta z = (\delta x(to)^T, \delta f^T(t_1), ..., \delta f^T(t_k), .., \delta b^T(t_1), ..., \delta b^T(t_k), ...)^T \tag{2}$$

which describes the increments of all control variables. In the incremental 4D-Var approach, we seek to minimize the quadratic cost function $J = J_b + J_o$, given by

$$J_b = \frac{1}{2}\delta z^T D^{-1} \delta z \tag{3}$$

$$J_o = \frac{1}{2}(G\delta z - d)^T R^{-1}(G\delta z - d) \tag{4}$$

where G is tangent linear model interpolated onto the observational space $d = y^o - H(x^b(t))$ are the innovation vectors of length N_{obs}, where **y^o** are observations and **H** is an operator that samples the nonlinear model trajectory at observational locations. **D** and **R** are the model background and observation error covariance matrices that will be discussed later. We seek an optimal solution for the increment to the control variable δz in equation (2), for which the total cost function **J** reaches a minimum value and the gradient of **J** vanishes. The optimal increment, referred to here as δz^a, is computed iteratively by solving a sequence of linear least squares minimizations (inner loops), repeated with periodic updates of **G** (outer loops). In ROMS 4D-Var a conjugate-gradient (CG) algorithm based on *Fisher* [1998] is used to achieve the minimization. The minimization procedure is terminated when $||\nabla J|| \leq \varepsilon$, where ε is the user-defined standard threshold for minimization. This typically requires a large number of iterations that are computationally prohibitive, so the numbers of outer and inner loops are fixed to yield a good estimate of the minimum **J** [e.g., *Broquet et al.*, 2009a]. During each inner loop, TLROMS is used to propagate the increments forward in time to evaluate (4), and ADROMS yields $\nabla J(\delta z)$, which is used by the CG algorithm to identify the minimum of **J**. In this study, the ROMS 4D-Var was allowed to adjust the initial conditions, boundary conditions, and surface forcing.

Zavala-Garay et al. [2012] compared the differences of tangent linear model and nonlinear integrations for an ensemble of slightly different initial condition to estimate the time over which tangent linear assumption is valid. It was found that the tangent linear assumption can be valid over a range of window length (1–10 days), a range that is confirmed by various other DA experiments [*Matthews et al.*, 2012; *Arango et al.*, 2011; *Powell et al.*, 2009]. For our experiment, we followed a similar DA set up of *Chen et al.* [2014] and used 3 day data assimilation windows that sequentially span the entire analysis period. At the beginning of each assimilation window, the initial condition derived from the last snapshot of previous DA window (or specified for the first window) is used to compute a forecast with NLROMS. This forecast provides the background trajectory, the DA 'prior'. If observations are available in the current assimilation window, then the ROMS 4D-Var inner loop starts with CG algorithm to yield an estimate of optimal increment δz^a, which is used to adjust control variables. The adjusted control variables are then used to compute the model trajectory after all outer and inner loops are completed within the assimilation window, the DA 'posterior' trajectory. Previous results suggest that the final cost function was similar irrespective of ways of combination of inner and outer loops [*Powell et al.*, 2008; *Broquet et al.*, 2009b]. In our case, we chose 1 outer loop and 20 inner loops for each DA window. We found that 20 loops are sufficient to yield a reasonable estimate of the minimum of *J*.

2.3. Assimilated Data
Various in situ and satellite-based observations were assimilated in this study, including:

2.3.1. NOAA CoastWatch Blended SST
The SST product (coastwatch.noaa.gov) is a blended product of SST observations from GEOS, AVHRR and MODIS satellites. This product is available daily from July 2002 to present with a spatial resolution of 10 km. As in *Chen et al.* [2014], an observational error of 0.4°C was chosen in this study.

2.3.2. In Situ Temperature and Salinity Time Series
These hourly profile data were measured with sensors on moorings of the Gulf of Maine Ocean Observing System (now part of the Northeast Coastal Ocean Observation System NERACOOS, http://www.neracoos. org, e.g., *Pettigrew et al.* [2011]). Temperature and salinity profiles from buoys F, I, M and N (Figure 2) were assimilated at 4 h intervals. Additional hydrographic data quality-controlled and archived by the UK Met Office Hadley Center (http://hadobs.metoffice.com/en3/data/EN3_v2a/) [*Ingleby and Huddleston*, 2007] were
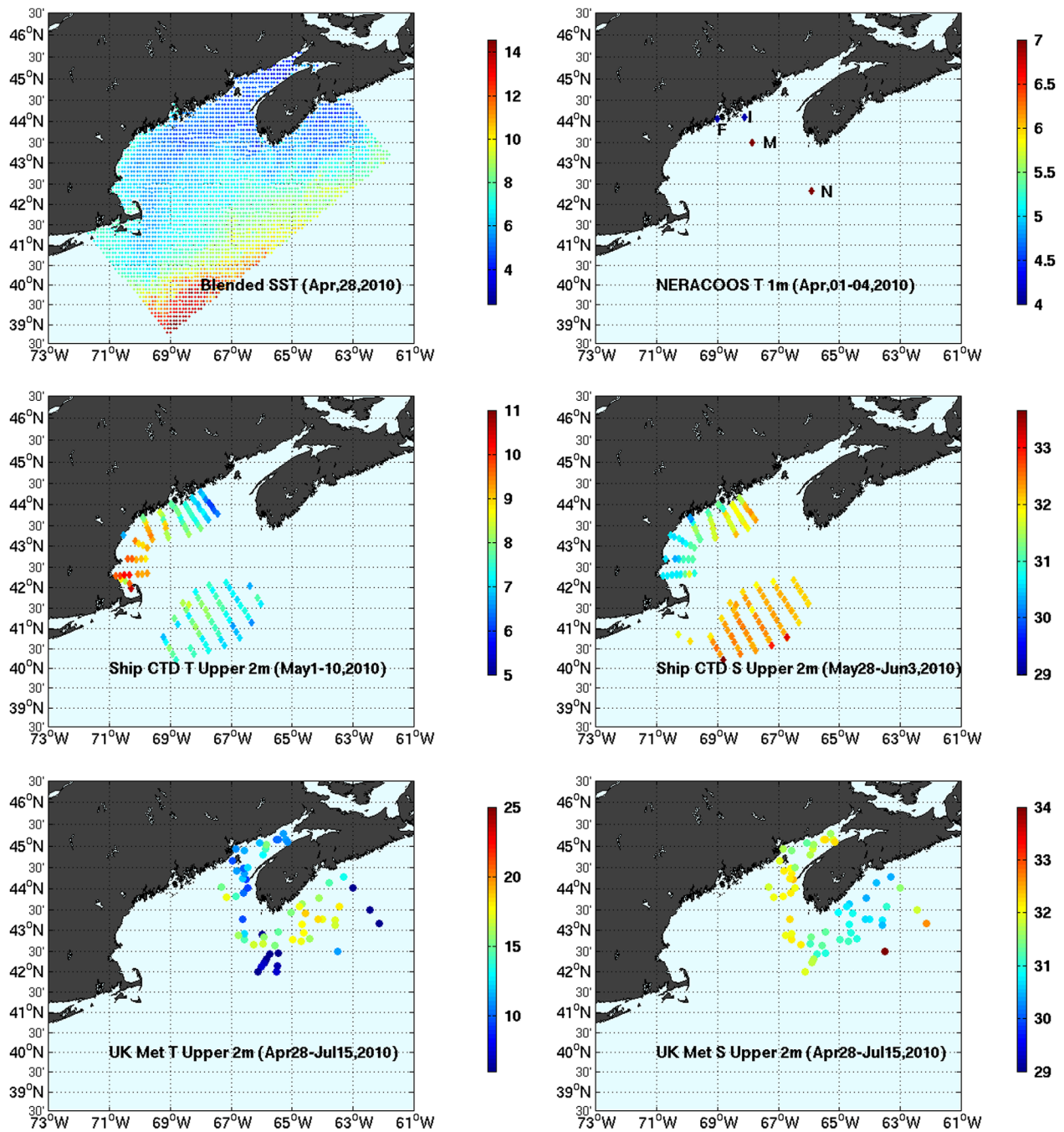
Figure 2. Observations assimilated into the GOM 4DVAR system: (a) Blended SST for 1 April 2010; (b) NERACOOS temperature observations at 1 m at 0:00Z 1 April 2010; Shipboard CTD observed (c) surface temperature for 1–10 May 2010, and (d) surface salinity for 28 May to 3 June 2010; (e and f) the locations for surface temperature and salinity observations collected by UK Met Office during 1 April to 18 July 2010. All temperature observations are in °C.

assimilated. These observations are derived from a variety of instruments and platforms, including expendable bathythermographs (XBTs), Argo floats, opportunistic surface themistor temperature measurements, and T/S profiles from the Global Temperature Salinity Profile Program (GTSPP). In this study, we used 0.1°C and 0.03 as the measurement errors for in situ temperature and salinity, respectively.

2.3.3. Shipboard CTD Data

CTD casts were collected during three GOMTOX surveys in 2010, including R/V *Oceanus* 465 (1–10 May), R/V *Endeavor* 460 (27 May to 3 June), and R/V *Oceanus* 467 (30 June to 8 July). CTD profiles ranged from 2 to
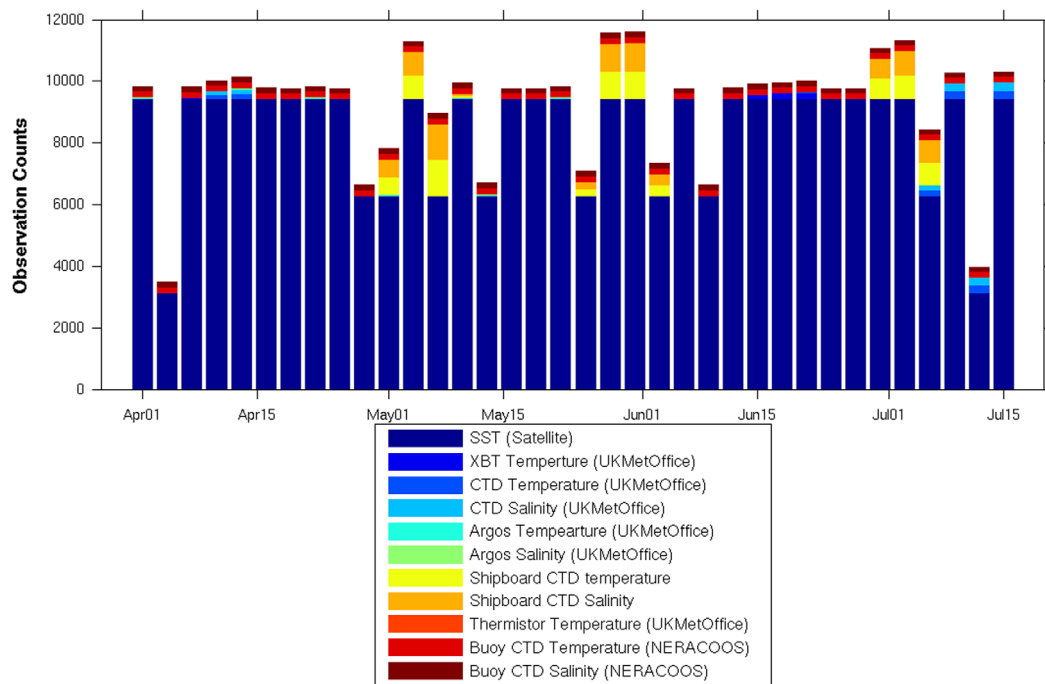
Figure 3. Temporal evolution of observation counts within each 3 day data assimilation window during 1 April to 18 July 2010.

200 m (or near the bottom for water depths less than 200 m), and we averaged all CTD data into 5 m bins. As for other in situ profile data, we used 0.1°C and 0.03 as the observational errors for temperature and salinity, respectively.

All observations were combined and averaged respectively to form "super observations," so that within each model grid cell and at each model time step, each state variable has only one observational realization. This procedure significantly reduces data redundancy, and the standard deviation of observations that contribute to each "super observation" was used as a measure of the error of representativeness. Given the uncertainties of altimetry data in coastal settings and the potential aliasing issue associated with the strong tidal flow in the GOM, we did not assimilate SSH data into the model. Previous work by various colleagues showed that the assimilation of along-track SSH is successful at various coastal seas, for example, off the Oregon coast [*Kurapov et al.*, 2011], for the Middle Atlantic Bight (http://marine.rutgers.edu/~wilkin/wip/espresso/espresso.html). Assimilation of SSH in such a coastal region with high tides such as GOM and BOF system remains a topic to be explored in the near future.

Example distributions of super observations of SST, UK MET office T/S profiles, NERACOOS buoy T/S, and ship CTD observations are shown in Figure 2. SST on the first day of DA cycle (1 April 2010) is shown, along with positions of all available in situ temperature and salinity profiles over the ∼110 day study period. The temporal distribution of super observations (Figure 3) indicates that the majority of observations feeding the DA system are satellite observed SST, which have a total of 2,83,050 data points. In situ NERACOOS buoy T/S profiles contribute a total of 11,754 observations. Shipboard CTD casts have a total of 15,462 observations. While the T/S profile data are less in number, they provide vital subsurface information to constrain model hydrodynamics.

2.4. Data Assimilation Setup

The model background error covariance matrix **B** determines the way that observational information is propagated to unobserved variables. Therefore proper definition of **B** has critical influence on the data assimilation performance. **B** contains the initial condition background (or prior) error covariance matrix $\mathbf{B_x}$, the open boundary condition background error covariance matrix $\mathbf{B_b}$, surface forcing background error covariance matrix $\mathbf{B_f}$. Each error covariance matrix can be expressed as $B = \sum C \sum$, where $\sum$ is the diagonal matrix of error standard deviations, and **C** is a univariate correlation matrix. The main source of background error is
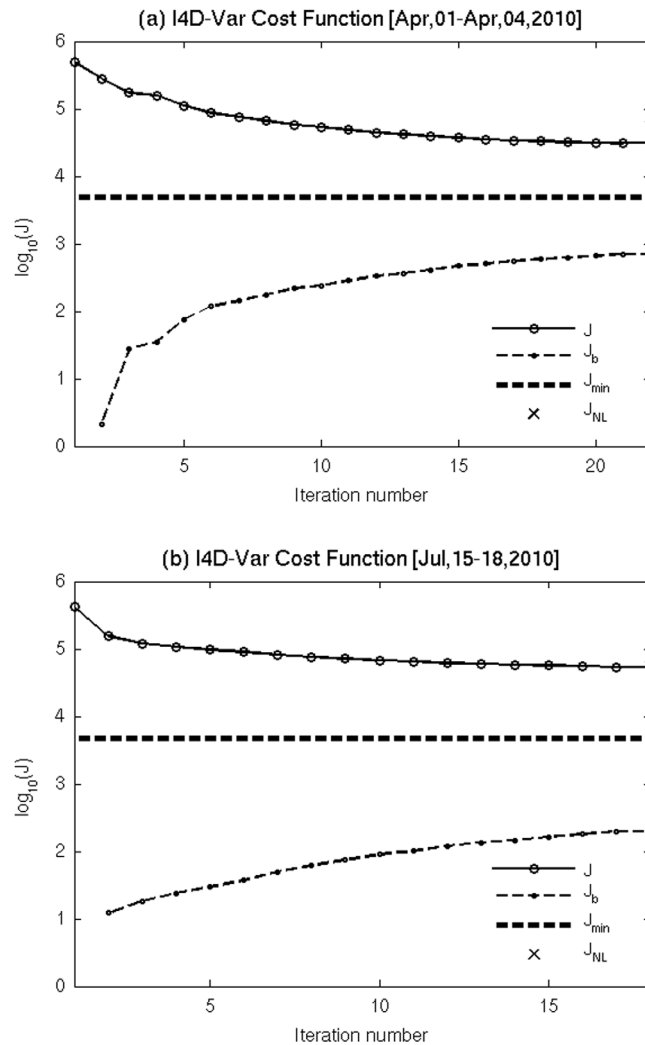
Figure 4. 4DVAR cost function (J) as a function of number of iterations of inner loops for (a) the first assimilation window (1–4 April 2010), and (b) last assimilation window (15–18 July 2010). Solid line with open circles is the total cost function (J), and dash dotted line is the background cost function (J_b). Theoretical minimum cost function ($J_{min=N_{obs}}/2$) is shown with a solid dashed line, and the cross represents nonlinear model cost function (J_{NL}) after data assimilation.

the model bias and spatial mismatch from observations. In this study, the standard deviation $\sum$ is computed on a monthly. For each month, $\sum$ is computed based on the temporal standard deviation of the corresponding detided 12 hourly GOM forward simulation solutions over 7 year period (2004–2010) during that specific month. The univariate correlation matrix is further factorized as $C = \Lambda L_v^{1/2} L_h^{1/2} W^{-1} L_v^{T/2} L_h^{T/2} \Lambda$, where Λ is a matrix of normalization coefficients, L_v (L_h) is the vertical (horizontal) correlation functions, and W is the diagonal matrix of grid volumes [*Moore et al.*, 2011a]. The correlation matrices, L_v and L_h, with their associated normalization factors Λ, were computed as solutions of diffusion equations following *Derber and Rosati* [1989] and *Weaver and Courtier* [2001]. The length scales chosen for L_v and L_h represent the decorrelation scales for a typical increment, and are currently assumed to be homogenous and isotropic. In our setup, the decorrelation length scales used to model the **B_x** were 50 km in the horizontal and 30 m in the vertical for all state variables. The correlation lengths of state variables for **B_b** were chosen to be 100 km in the horizontal and 30 m in the vertical. The horizontal correlation scales for **B_f** were set as 100 km for background surface tracer and momentum fluxes. Those values are comparable with *Moore et al.* [2011b] and *Chen et al.* [2014] and are reasonable since our focus in on the gulf-wide coastal circulation in the GOM.

3. Results

3.1. Cost Function Reduction

The performance of the GOM 4D-Var system can be first evaluated by the reduction of the cost function (Figure 4). During the first assimilation window (1–4 April 2010), the total cost function is effectively reduced in the first 7 inner loops, with reductions ranging from more than 30% to about 5%. After the 16 inner loops, the reduction of cost function stays below 5% and approaches zero in the 20th loop, suggesting that 20 inner loops are sufficient to yield a good minimization of cost function. The theoretical minimum value J_{min} of total cost function J would have a mean of $N_{obs}/2$ [*Weaver et al.*, 2003], in which N_{obs} is the number of assimilated observations in each window. In our case, after 20 loops, the cost function is indeed asymptotic near the theoretical value. The total cost function (Figure 4) in the last assimilation window (15–18 July 2010) is smaller than that in the first window. The final value of J also approaches the J_{min}, indicating a good fit to the observations. Overall, a reduction of ~90% of the total cost function is achieved in window 1 and window 36, respectively. The fact that the final nonlinear cost function approximately coincides with J
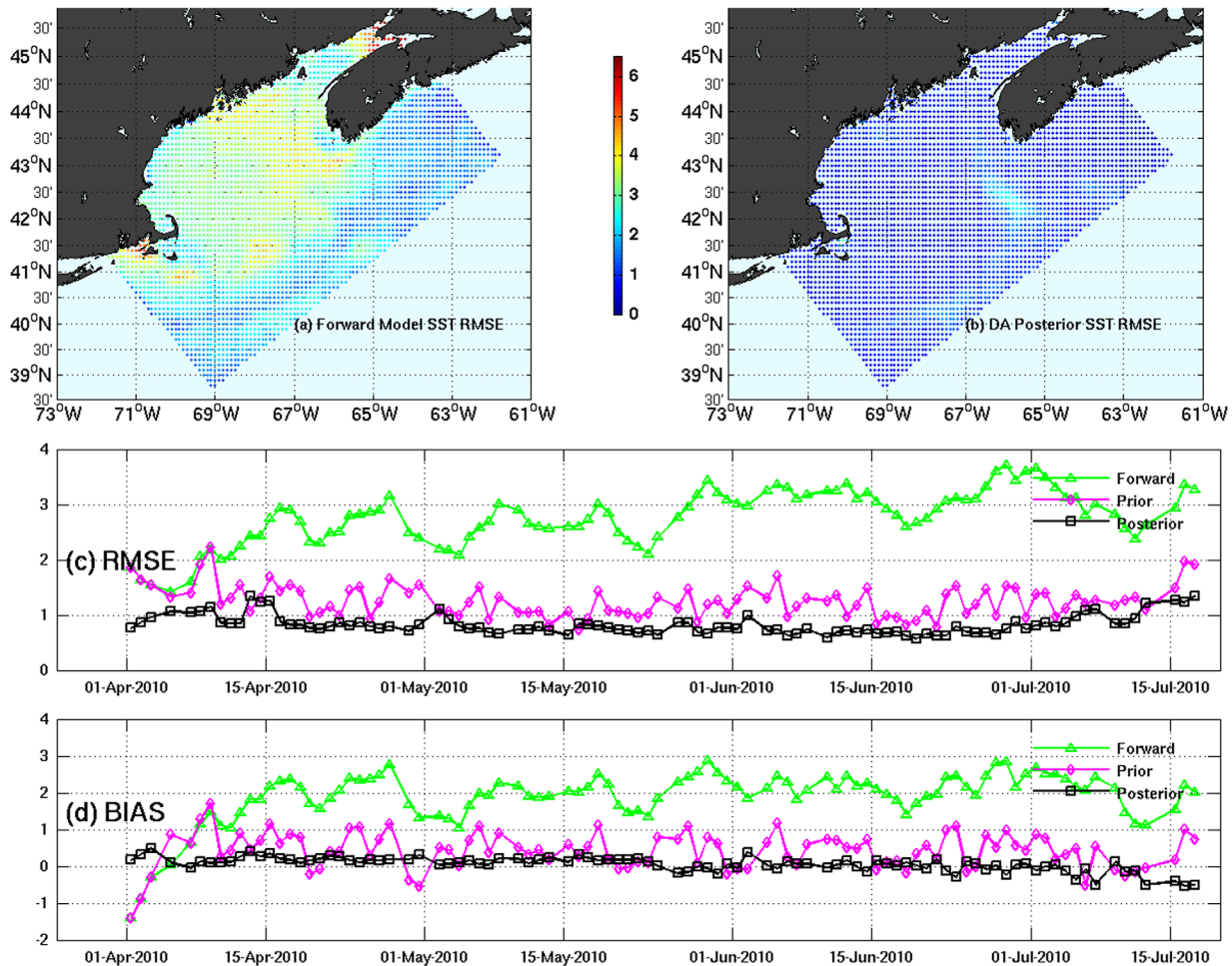
Figure 5. Spatial distribution of the temporal SST root mean square error (RMSE) between observations and (a) the forward model solution and (b) the DA posterior solution. Temporal evolution of the SST RMSE (c) and bias (d) for the forward model, the prior, and DA posterior.

value indicates the choice of using 3 day as the assimilation window for tangent linear approximation is reasonable.

The behavior of the cost function depends on both D and R (equations (3) and (4)). In our DA experiments, the observational cost function J_o is much larger than the background cost function J_b ($J_o \sim 10\, J_b$, Figure 5). By the 20th iteration, both J and J_b approach asymptotic values, achieving a balance between departures from the model background state and fitting the observations [e.g., *Broquet et al.*, 2009a]. Sensitivity experiments show that the termination of DA at 20th loop prevents excessive divergence of the model from the basic state while still ensuring a good fit to observations. The overall performance of the cost function during the hindcast period shows our choice of background error and observational errors are appropriate.

3.2. Effectiveness of the 4D-Var Algorithm
3.2.1. Surface Performance
The forward model contains large root mean square errors (RMSEs) in SST in regions near Nantucket Island, Georges Bank, the eastern GOM, and the BOF where there is strong tidal mixing (Figure 5a). The RMSE is significantly reduced after data assimilation (Figure 5b). The maximum RMSE value of the posterior solution is less than 3°C (as opposed to a maximum of 6°C in the forward simulation). The performance of DA system was also evaluated in time series of spatial RMSE, based on model realizations at all assimilated observation locations. As shown in Figure 5c, the RMSE between the forward model and observations ranges from 1.5°C
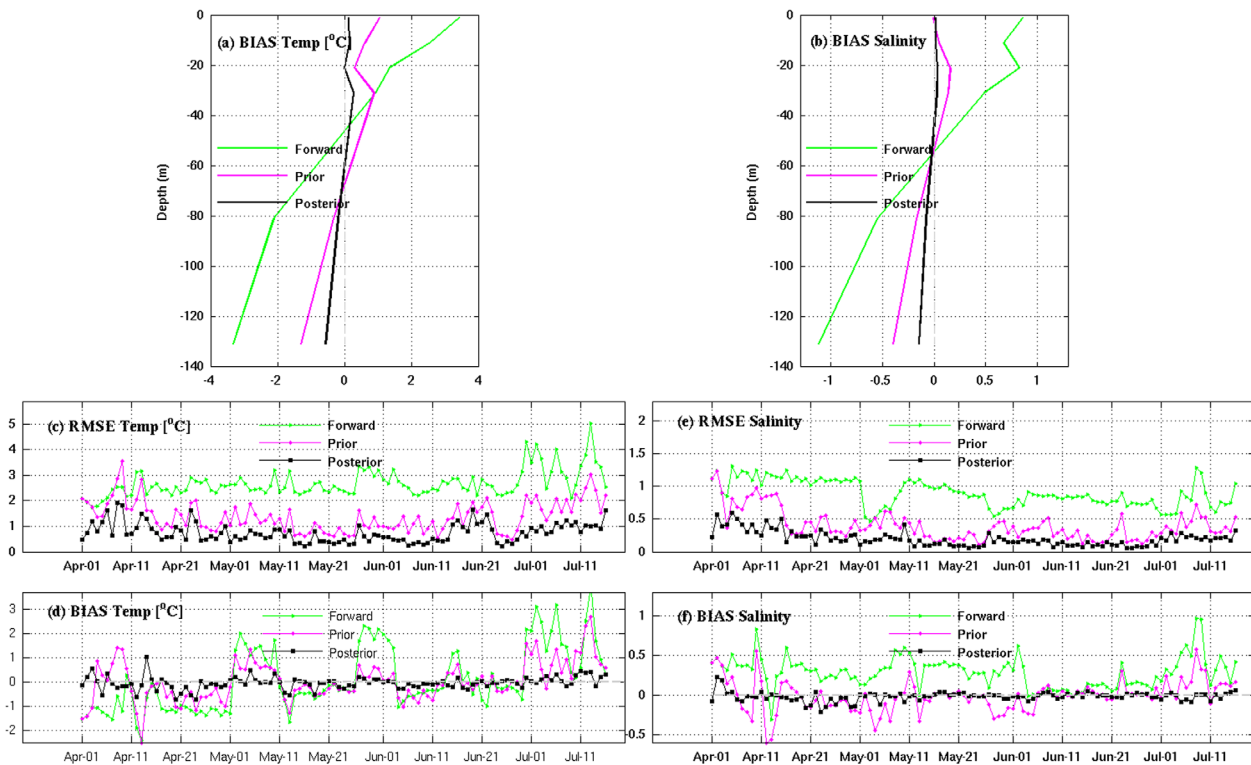
Figure 6. (top) Vertical profiles of (a) temperature and (b) salinity bias between assimilated observations, forward and DA posterior model solutions. (bottom) Temporal evolution of subsurface temperature and salinity RMSE and bias.

to more than 3°C. By assimilating surface SST data, the RMSE was effectively reduced throughout the region. The DA prior RMSE is around 1.5°C, and the DA posterior SST RMSE is less than 1°C.

In addition to RMSE, we also computed the model-observation error bias to provide more specific information on whether the model overestimates or underestimates observations. The forward simulation has ∼1.5°C bias, overestimating SST throughout the observational period (Figure 5d). This bias is reduced to near zero in the DA posterior simulation. We note that in some cases, the DA posterior had worse RMSE/bias than the prior. For instance, the posterior RMSE on 13 April and 13 July is slightly larger than the prior. To understand why this can be the case, it is important to remember that 4D-Var is minimizing the overall misfit between the model and observations. In some circumstances, the overall minimization can lead to degradation of individual components of the fit. Such situations can be exacerbated by inconsistency among assimilated data sets (satellite SST versus CTD-based temperature) and differences in observational errors among state variables (temperature versus salinity). In addition, we used blended SST data to assimilate into the modeling system. Blending microwaved and infrared (IR) SST data enables greater coverage and higher accuracy than IR only SSTs, but current objective-interpolated SST does not completely eliminate cloud contamination inherent to IR SSTs. Therfore, it is possible that its observational error can be greater than that is used in the DA (0.4°C). Nevertheless, over the course of the simulation period, the DA posterior solutions provide realizations of surface temperature that are much better overall than the forward model and the DA prior.

3.2.2. Subsurface T/S Statistics

The effectiveness of 4D-Var data assimilation was further evaluated against subsurface hydrographic observations. Near the sea surface, the forward solution has a temperature bias of 2°C (Figure 6a), which is roughly one degree less than that for the surface based on satellite data. The temperature bias decreases with depth and becomes negative around ∼ 50 m. By 90 m, the temperature bias exceeds −2°C. The vertical distribution of temperature bias suggests the forward model overall overestimates (underestimates) observed temperature in upper (lower) water column. Data assimilation significantly reduces these biases.
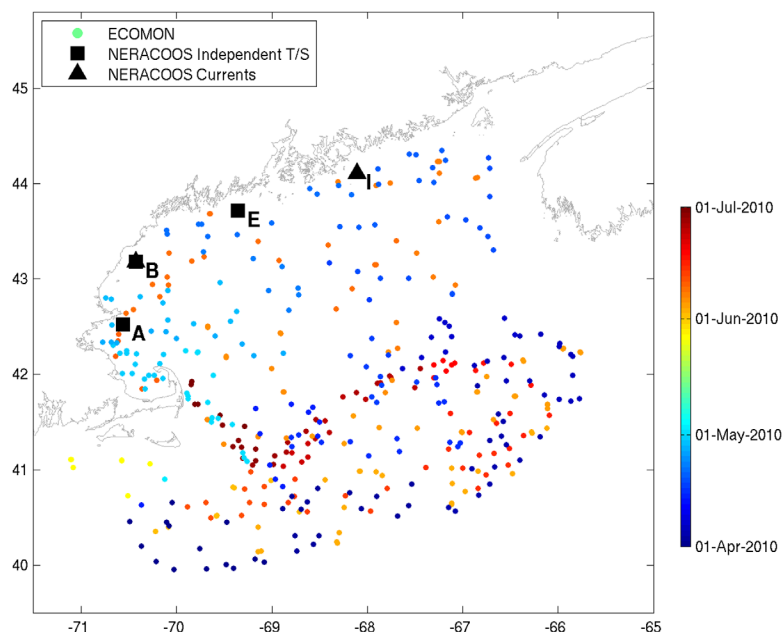
Figure 7. Station locations of CTD casts from the Northeast Fisheries Science Center ECOMON ship survey data (circles color-coded by date) within the model domain during 1 April to 18 July 2010. Also shown are the NERACOOS moorings used for independent comparisons. Specifically, buoys A, B, and E (black squares) are used for T/S comparisons, and buoys B and I are used for ocean current comparisons.

The temperature bias in the DA prior simulation is ~1°C, which is further reduced to ~ 0.3°C in the DA posterior simulation.

Similar improvement is seen in salinity (Figure 6b). The forward simulation overestimates the upper water column salinity by ~ 0.8 and underestimates the salinity at depth by ~ 0.8 or more. After data assimilation, the upper water column salinity bias is reduced to ~ 0.1 or less and the subsurface bias is reduced to less than 0.2.

Time series of spatial RMSE between model and observations (Figures 6c and 6e) showed the temperature (salinity) RMSE is reduced from 2–3°C (0.5–1) to ~1°C (0.2), suggesting DA posterior produces more accurate subsurface information. Time series of the spatial bias (Figures 6d and 6f) provides yet another view of the performance of data assimilation. The temperature bias (Figure 6d) in the forward simulation ranges from −1.8°C at the beginning of the study period to 2.5°C at the end of study period. This bias in temperature is effectively reduced after data assimilation. Both the DA prior and posterior simulations show that the temperature bias is reduced to a much smaller range, between −0.8°C and 1°C. Similar improvement is evident also for salinity (Figure 6f). After data assimilation, the salinity bias is reduced to close to zero over the entire assimilation period, as opposed to up to 0.8 in the forward simulation.

Overall, our comparisons indicate the 4D-Var is effective in reducing the misfits between model and assimilated observations. Although most of data being assimilated are satellite SST (Figure 3), our results show the assimilation also improves the model's fidelity in resolving subsurface hydrographic conditions.

3.3. Validation Against Independent Observations
A more rigorous evaluation of the data assimilative simulation can be achieved by comparing model fields with independent observations (i.e., data that have not been assimilated). Spatial distributions of these independent data are shown in Figure 7, including ocean velocity observations measured by NERACOOS coastal buoys B (WGOM), and I (EGOM), and CTD temperature and salinity at 2 m, 20 m and 50 m at buoys A, B, and E in the WGOM. Temperature and salinity profiles from the NOAA Northeast Fisheries Science Center (NEFSC, http://www.nefsc.noaa.gov/epd/ocean/MainPage/ioos.html) Ecosystem
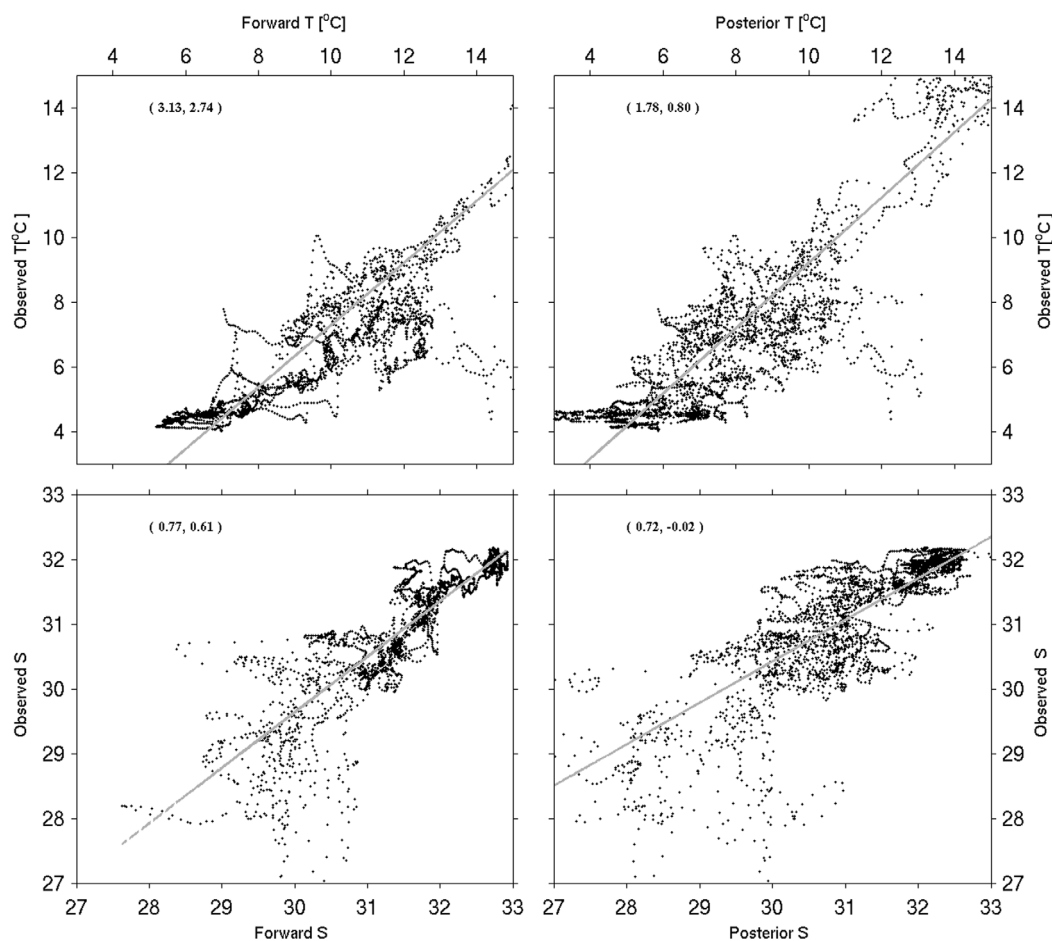
Figure 8. Scatter plots of observed versus modeled (top) temperature and (bottom) salinity at buoys A, B, and E (forward model in the left column, posterior in the right). The gray lines are linear fits for each scatter plot. Doublets in the brackets are model-data RMSE and bias, respectively. The moored observations were not assimilated into the model, and are used only for model evaluation.

Monitoring (ECOMON) shelf surveys during 1 April to 18 July 2010 were also used to validate the DA model solutions.

3.3.1. Comparisons With NERACOOS Buoy T/S

Direct point-by-point comparison was made to estimate the DA model skill in reproducing the hourly temperature and salinity data at NERACCOS buoy A, B, and E (Figure 8). The forward model overestimates the observed temperature (salinity) by 2.7°C and 0.6, with an RMSE of 3.1°C and 1.8, respectively. Compared to the forward model, the DA posterior simulation provides better agreement for both temperature and salinity. The model-data biases are reduced to 0.8°C and −0.02 for temperature and salinity, respectively. For temperature (salinity), RMSE between model and observations are reduced to 1.8°C (0.7) after DA.

3.3.2. Comparisons With the NEFSC Data

The NEFSC data have wider range of spatial coverage, and in total, 399 temperature and salinity profiles are available for comparison. We note that among these observations, 1–10 April, 1–15 June are two periods when sampling occurred in water depths exceeding 200 m, where warm and salty slope waters permeate the Northeast Channel (NEC), northern flank of Georges Bank, as well as Jordan and Wilkinson Basins (Figure 9).

The initial NEFSC survey on 1–10 April (observation numbers 1–69) was conducted from the Great South Channel to the NEC. CTD data show that the bottom waters (greater than 50 m) had temperature exceeding ∼13°C and salinity as high as 36. The forward model simulation tends to overestimate surface temperature by over 1°C but underestimates the subsurface temperature even more significantly. The bottom salinity is
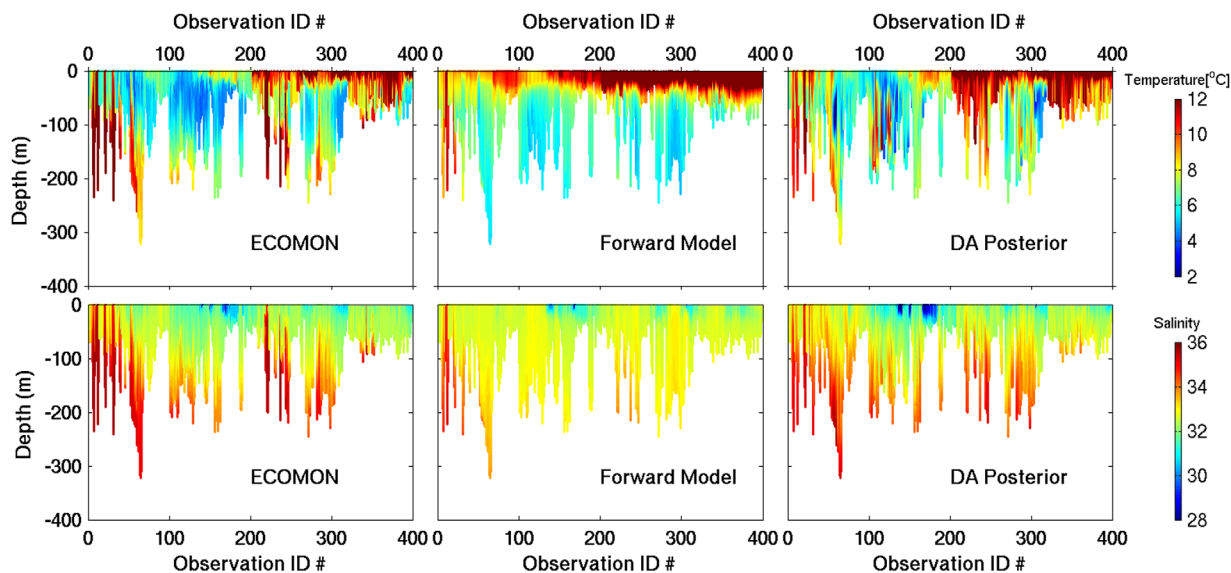
Figure 9. Comparisons between (left column) NEFSC ECOMON temperature and (middle) salinity data and forward model and DA posterior counterparts. The X axis is observation identification number in chronological order. See Figure 7 for station positions.

also 1 unit fresher than the observations. After DA, simulated bottom water temperature and salinity compare more favorably with in situ T/S data.

In near-coastal regions sampled from mid-April to May (observation numbers 70–209), NEFSC data show an obviously freshening in the upper column. In the forward model, surface temperature is overestimated, whereas bottom temperature is underestimated. DA solutions have much better agreement with observations. During the first 2 weeks of June (observations 210–343) stations were concentrated in the interior GOM, including Jordan and Wilkinson Basins. The forward model simulation fails to capture the deep ($>$ 100 m) warm and salty waters, and overestimates the surface layer ($<$ 100 m) temperature by 1°C. In late June and early July (observation numbers 344–399), the forward model also fails to capture the warm and salty water near Georges Bank. All of these deficiencies are corrected in the DA simulation. The aggregate temperature and salinity RMSEs are reduced from 3.21°C to 2.05°C and from 0.90 to 0.64, respectively, representing a roughly 40% error reduction in the DA simulation.

Point-by-point comparisons along with linear fits show the DA model skill improvement in resolving observed temperature and salinity characteristics (Figure 10). The DA posterior solutions show much better agreements with observations than the forward model. The regression slopes for temperature and salinity are closer to one, and the intercepts are smaller as well. All these results suggest that the DA model significantly improved the subsurface ocean state estimation.

Coastal velocity time series comparisons also show significant skill improvement in the DA posterior. For example, before DA the forward model simulated current at buoy B displays a strong and relatively persistent northward current in April and early May that is not observed (Figure 11). The DA posterior fixes the issue, and also improves some aspects of the temporal variation of the currents in the eastern GOM. The complex correlation coefficients between observed and model velocity time series increase from 0.3 for the forward model simulation to 0.8 for the DA posterior simulation. The average angular difference drops from 7° in the forward model to 2.5° in the DA solution. Similar improvement is also found for buoys I in the eastern GOM.

In summary, model comparisons against independent hydrographic and velocity data show that the gulf-wide ocean state is overall more accurate in the DA posterior solutions than both the forward model and the DA prior.

4. Discussion

Assimilation of data allowed the model to capture an anomalous water mass that impacted both the physics and biology of the Gulf of Maine in 2010 [*McGillicuddy et al.*, 2011]. To better understand the source
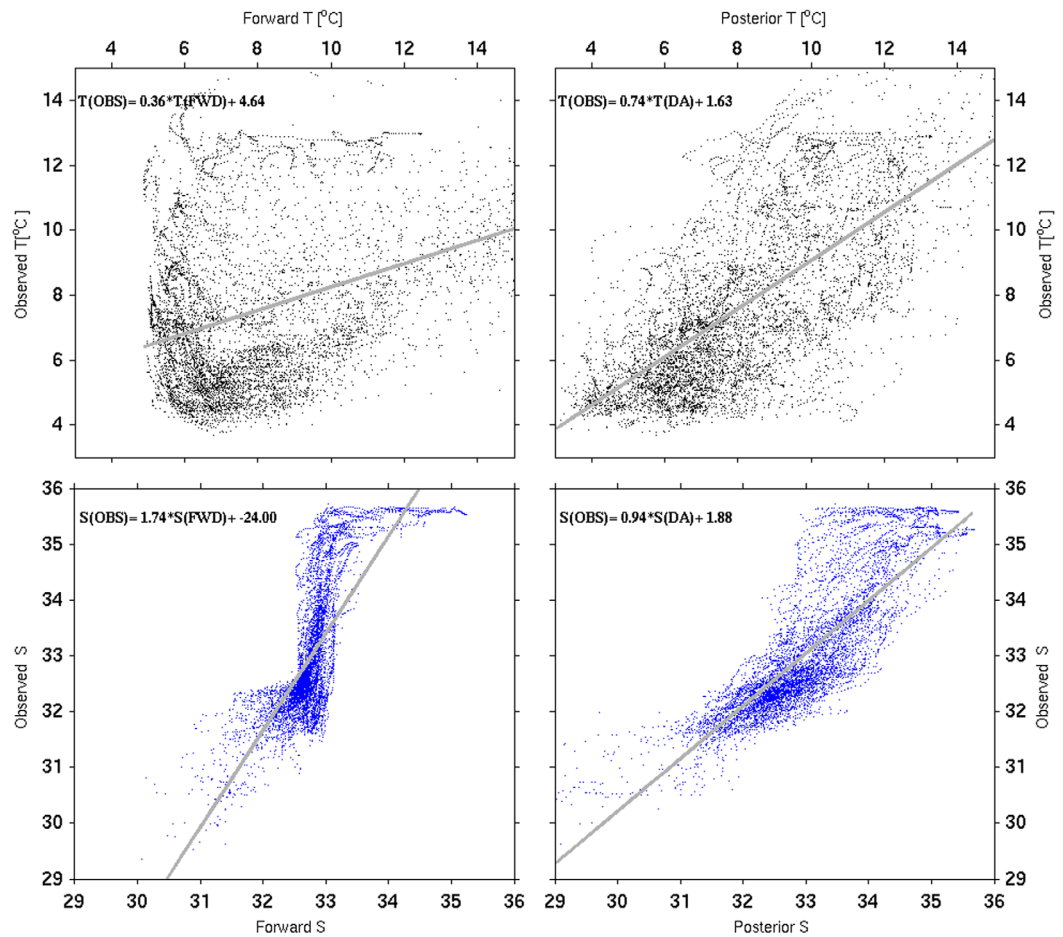
Figure 10. Scatter plots of simulated versus observed NEFSC ECOMON (top row) temperature and (bottom row) salinity, with the forward model in the left column and posterior in the right. Gray lines show linear fits for each scatter plot (slope and intercepts indicated in insets).

of that water mass anomaly, we undertake a detailed analysis of the heat budget for the DA posterior and compare it to the forward model (section 4.1). We then diagnose its impact on the circulation (section 4.2), and investigate the advective connection with one of the apparent source regions on the Scotian Shelf (section 4.3).

4.1. Heat Budget Analysis

To analyze the relative contribution of surface heat flux and advection to the temperature variability in forward and DA posterior solutions, we can diagnose the temperature equation following *He and Weisberg* [2002]:

$$\underbrace{\frac{\partial T}{\partial t}}_{(a)} = -\underbrace{(u\frac{\partial T}{\partial x} + v\frac{\partial T}{\partial y} + w\frac{\partial T}{\partial z})}_{(b)} + \underbrace{\frac{\partial}{\partial z}(K_H\frac{\partial T}{\partial z})}_{(c)} + \underbrace{\frac{\partial}{\partial x}(A_H\frac{\partial T}{\partial x})}_{(d)} + \underbrace{\frac{\partial}{\partial y}(A_H\frac{\partial T}{\partial y})}_{(e)} \tag{5}$$

where T is the temperature, u, v, w are the velocity, and K_H the vertical diffusivity coefficient. A_H is the horizontal diffusivity coefficient. Term **(a)** represents the local time rate of change, **(b)** the advective rate of change, and **(c)** the vertical diffusion. The horizontal diffusion terms (d)+(e) are an order of magnitude less than the vertical diffusion and are therefore not considered. In the depth-averaged sense, (5) can be rewritten as:

$$\underbrace{\frac{\partial T}{\partial t}}_{(a)} = -\underbrace{(u\frac{\partial T}{\partial x} + v\frac{\partial T}{\partial y})}_{(b)} + \underbrace{\frac{Q(t)}{\rho C_p H}}_{(c)} \tag{6}$$
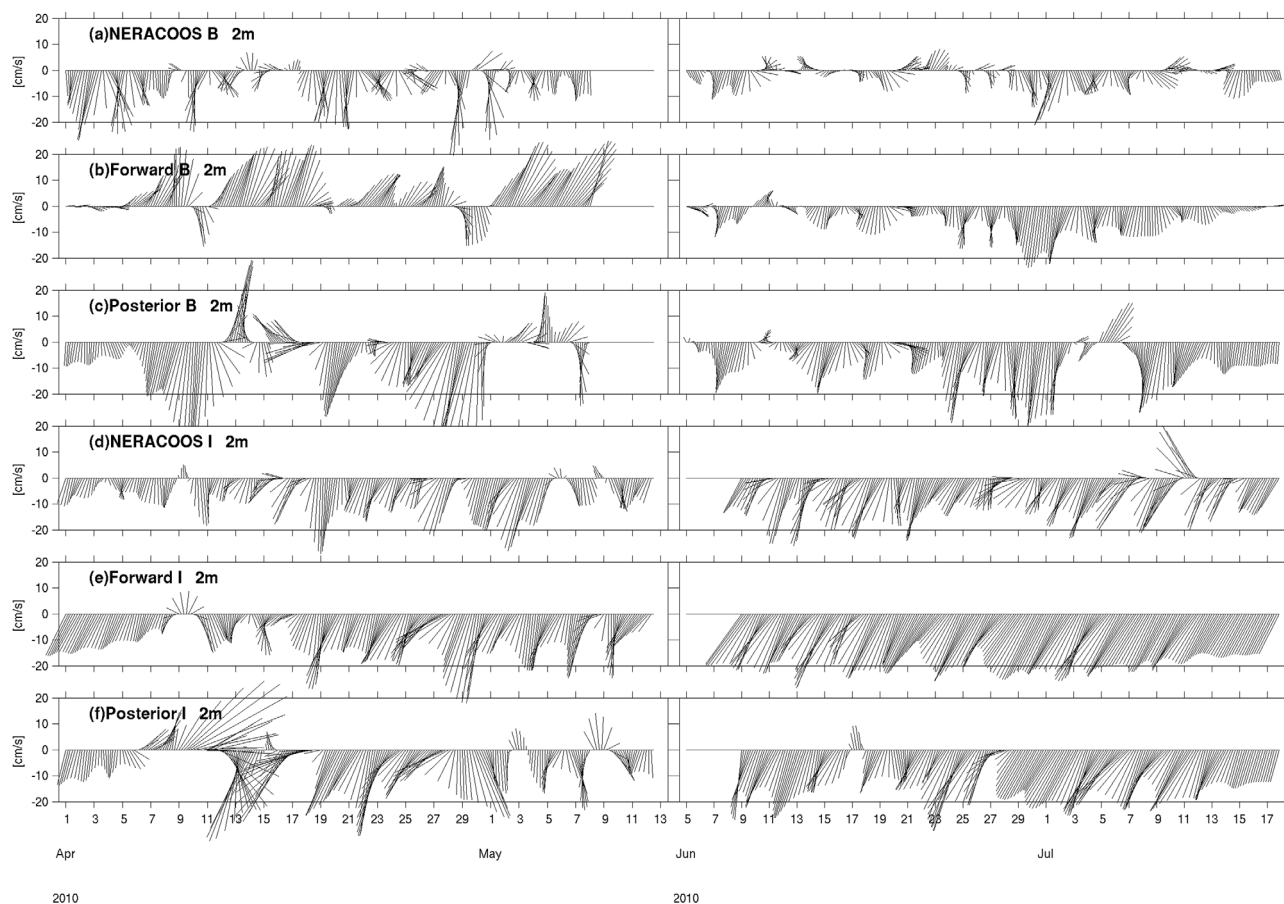
Figure 11. Comparisons of 2 m surface currents between observations and model forward and posterior solutions for buoy B in the western Gulf of Maine and buoy I in the eastern Gulf of Maine. The sample frequency is 4 hourly, and all time series are 36 hourly low-pass filtered to extract the subtidal currents. Note the 1 month break in the time series dictated by data availability.

where T is the depth-averaged temperature, Q is the net surface heat flux, H is the water depth, and ρ and C_p are sea water density and specific heat capacity respectively.

We diagnosed the contributions of the advection term **(b)** and heat flux term **(c)** in determining temperature changes during summer 2010. To show the result, we averaged equation (6) in time from 1 April to 18 July 2010. In the forward model, the depth-averaged advection term (Figure 12a) is negative in the offshore area near majority of the slope region and Scotian Shelf, and is largely negative near Cape Cod. The value is positive in the EGOM, BOF and Jordan Basin, suggesting the contribution from advection is to increase the water temperature in these regions. The DA posterior (Figure 12c) shows an overall similar spatial pattern, but the positive values are confined to Jordan Basin, the slope sea, and the BOF. The difference between posterior and forward terms (Figure 12e) reveals negative anomalies in the advection term in the WGOM, Georges Bank and BOF. This suggests that the advective contribution in the posterior tends to decrease the warming trend in these areas. In contrast, the advection term in Jordan Basin, the Scotian Shelf, and the continental slope is positive, thus favoring an elevated rate of change. The magnitude of the heat flux term (Figures 12b and 12d) is overall larger than the advection term in the shallow coastal region in water depths less than 100 m, especially in the BOF and on Georges Bank where tidal mixing is strong. The difference between the DA posterior and forward model solutions in heat flux term (Figure 12f) is positive on Georges Bank and in the BOF. We also note negative values on the Scotian Shelf, suggesting there is a major adjustment of the heat flux term near the eastern boundary. As such, we conclude that both advection and surface heat flux play important roles in correcting the temperature bias in the forward model. Adjustment to the advection term (Figure 12e) is larger than the heat flux adjustment (Figure 12f) in regions with strong tidal mixing, such as Georges Bank and the BOF.
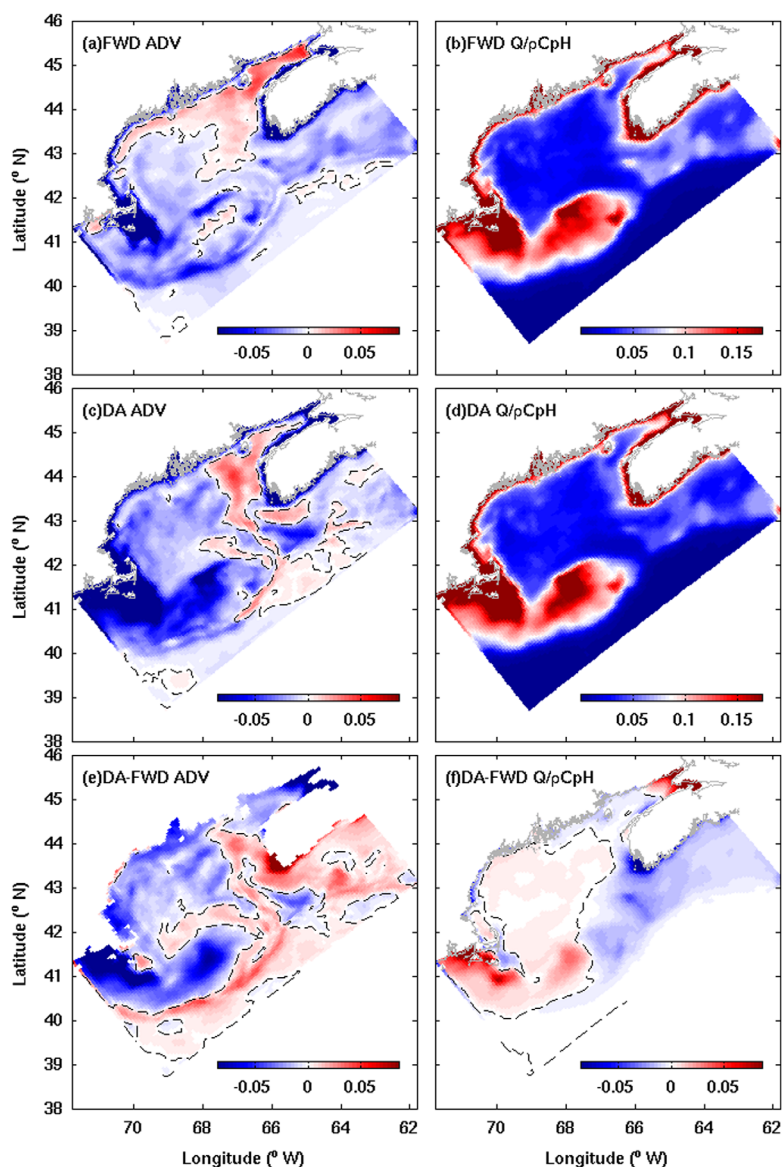
Figure 12. Term-by-term diagnostics of depth-averaged temperature budget. (a and b) Advection and heat flux terms for forward model, and (c and d) the DA posterior counterparts. (e and f) The differences between the DA posterior and forward model. Dotted gray lines are the zero contours in each plot. Units for each plot is $°C\ d^{-1}$.

4.2. Evolution of the Hydrography and Coastal Circulation in the GOM

The DA model solutions enable us to analyze the hydrographic variability in the GOM in spring-summer 2010. Monthly mean surface temperature and salinity maps (Figure 13) show some noticeable differences between forward and DA posterior solutions. The surface temperature field produced by the DA simulation is ~1°C cooler than those produced by the forward simulation. Surface salinity fields produced by the DA simulation are generally fresher than the forward model in the interior of the Gulf of Maine. Salinity in the DA solution is also fresher in the Scotian Shelf inflow region, suggesting a correction to the boundary salinity fluxes that in turn affects the interior salinity fields. Near the southeastern flank of the open boundary on the continental slope, salinity in the DA posterior is higher than that of the forward model in May–July, suggesting a possible intrusion of salty slope waters cross the model's deep ocean boundary. At the bottom of ocean (Figure 14), temperature in the NEC and in Jordan Basin is 0.6°C warmer after DA, due to the assimilation of buoy M and N temperature which is representative of slope water (upper panel, Figure 14). Without DA, more saline water (salinity>35) [*Smith et al.*, 2001] is only
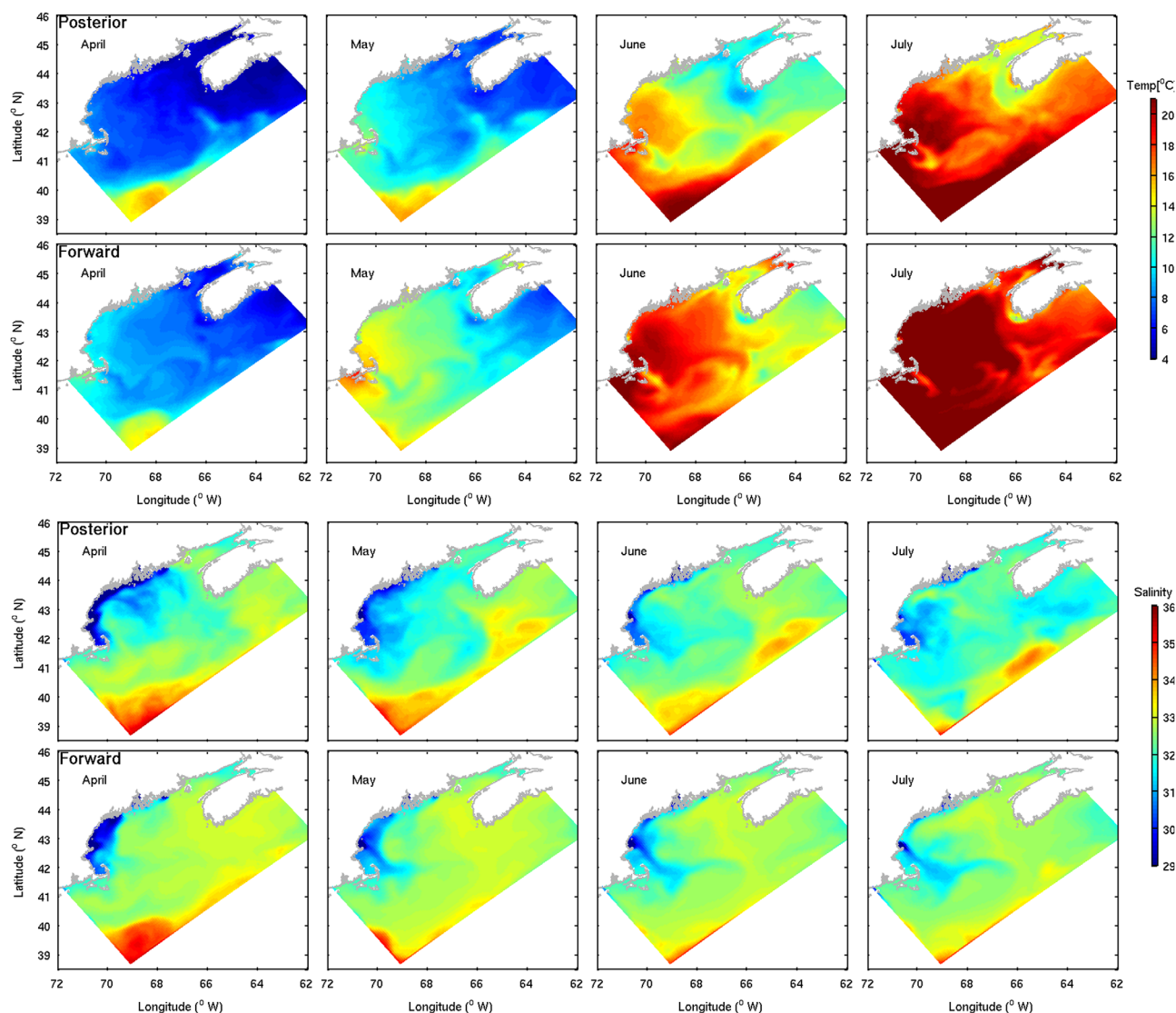
Figure 13. Monthly averaged modeled surface temperature and salinity for both forward and DA posterior solutions.

present in the slope region and southwestern portion of Wilkinson Basin. After the DA, salty slope water is found in both Jordan and Wilkinson Basins. The warm and salty slope water is present from the onset of model simulation (1 April) through July. Analysis of the observed T/S data from buoy M in Jordan Basin suggests that the slope water intrusion was initiated in late fall 2009 [*McGillicuddy et al.*, 2011], long before the initialization date of the present model.

The impact of water mass change on the gulf-wide circulation is presented in Figure 15. Compared to the surface circulation produced by the forward simulation, the DA solution presents a great portion of the coastal currents veering offshore of Portland Harbor in April, resulting in a significant reduction in the along-shelf transport in the WGOM (not shown). In May, the DA simulation shows that a semi-closed gyre is present in Jordan Basin and the eastern GOM, connecting the eastern GOM coastal waters with the Scotian Shelf and the Bay of Fundy. Such a current feature may facilitate the delivery of fresh water from Scotian Shelf into the Gulf. Surface elevation offshore of Penobscot Bay increases compared to the April condition (not shown). The resulting pressure gradient between Penobscot Bay and the Jordan Basin increases, leading to a stronger cyclonic gyre that helps to move coastal water offshore. The current in the western GOM becomes less organized in June (Figure 15) and July (not shown). This is consistent with geostrophic transport calculation and ADCP observations reported in *Li et al.*, [2014a].
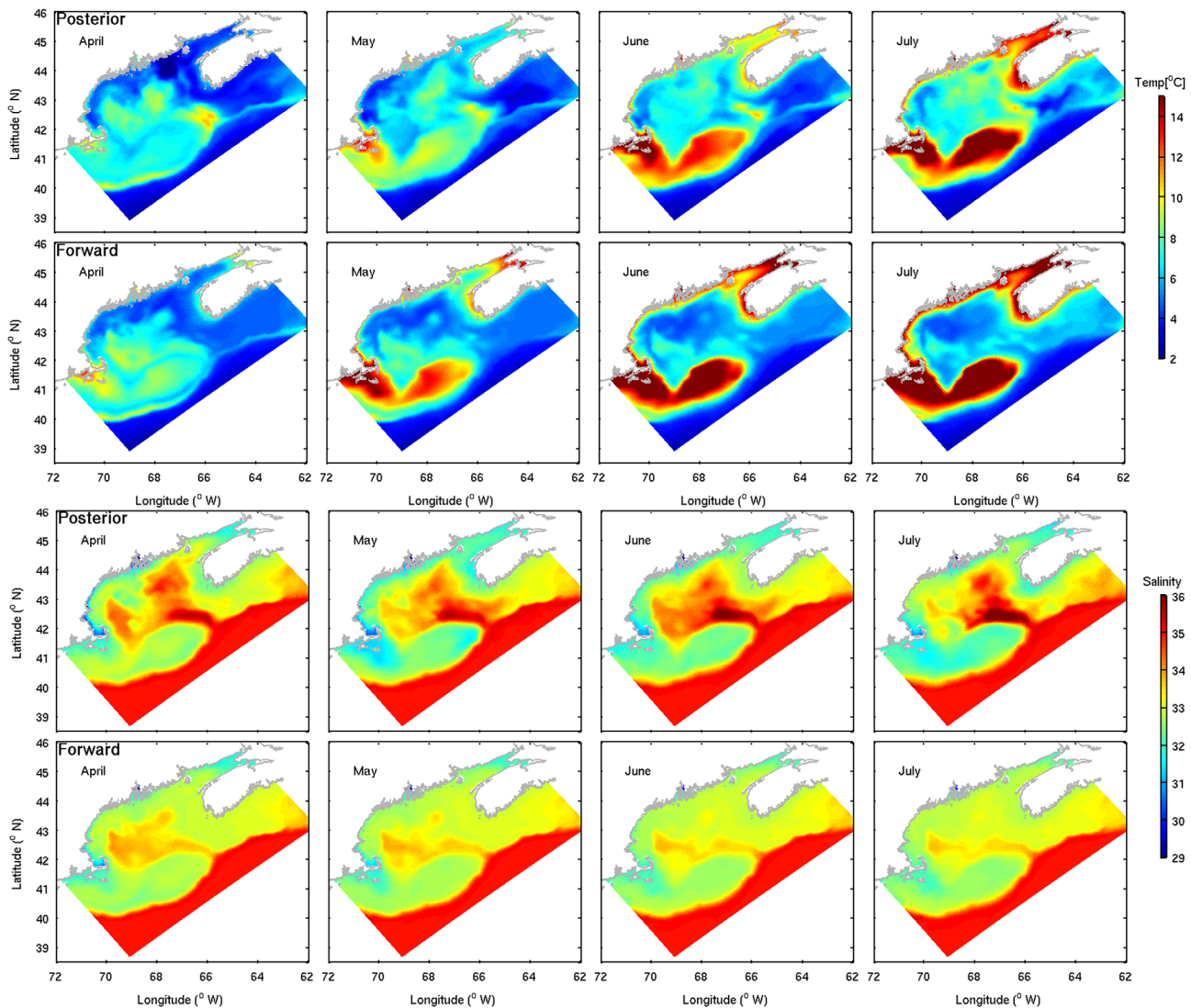
Figure 14. Monthly averaged model trajectories for the bottom temperature and salinity for forward and posterior model solutions.

Apparently, the sea level depression southwest of Jordan Basin plays a critical role in modulating the connectivity between western and eastern GOM coastal circulation.

4.3. Advection Time Scale From the Scotian Shelf to the Coastal GOM

Freshening of the Gulf of Maine in the DA posterior is apparently linked to the cold low-salinity water entering from the Scotian Shelf. Observations from Canadian Atlantic Zone Monitoring Program (AZMP) indicate that the SSW was colder and fresher than usual in 2010 compared to other years. The onset of the anomaly can be traced back to January 2010 at AZMP station 2 off Halifax [*McGillicuddy et al.*, 2011]. Similar water mass properties are also found in the upper 50 m of the NERACOOS buoy M in the Jordan Basin throughout the spring and summer [*Li et al.*, 2014a]. It is therefore of interest to investigate the advection time scale of SSW transport to Jordan Basin. The transit time is estimated using passive particle releases initiated throughout the water column from the Scotian Shelf using the space-time continuous DA model simulated current field. In order to be representative of Scotian Shelf water properties, a rectangular area was selected for release points (Figure 1, gray dots), and vertical depths are chosen between the ocean surface (0 m) and 200 m with a 10 m spacing. A total of $N_o=8111$ particles are released from 1 April 2010, the starting date for the model simulation, and are allowed to advect to the end of the simulation (18 July 2010). At each
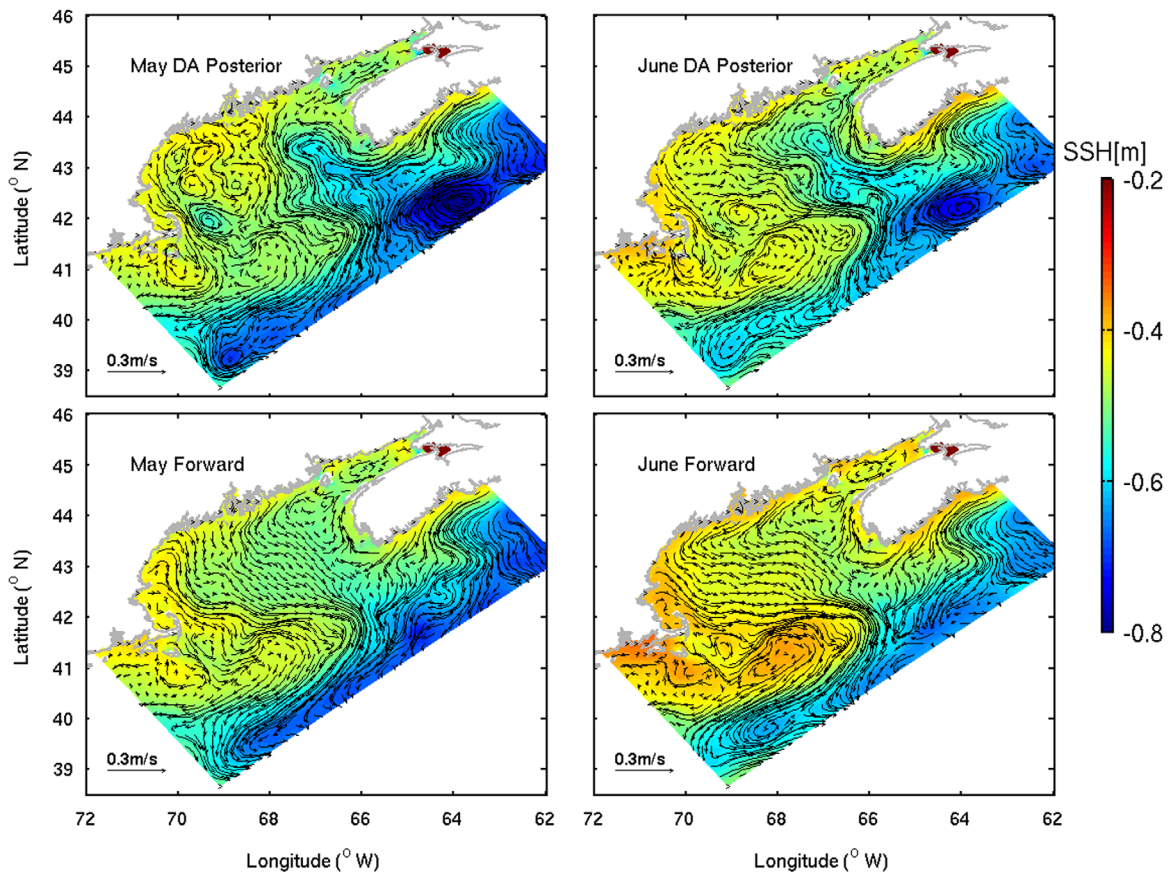
Figure 15. Monthly mean model trajectories for the surface currents for model forward and posterior model solutions in May and June. A current scale of 0.3 m s^{-1} is also shown.

time t_i, we first count the number of particles inside each polygon (N) designated for Jordan Basin. The advection time scale τ can be estimated as:

$$\tau = \left(\sum_{i=0}^{\infty} t_i \cdot \frac{N_i}{N_o}\right) / \left(\sum_{i=0}^{\infty} \frac{N_i}{N_o}\right) \tag{7}$$

where i is the index for each time level. Particles (not shown) started to enter Jordan Basin after 20 days, and reached a peak in May to late June. There was a gradual decrease of the percentage as the season progresses. Applying equation (7) to Jordan Basin by integrating t_i from zero to the available length of the simulation window (105 days) gives the mean advection time τ of 59 days. The advection time scale is consistent with estimates from in situ observations, although the onset of the water mass anomaly began prior to the time period of the present simulation [*McGillicuddy et al.*, 2011].

5. Summary and Future Work

In this study, the recently developed strong constraint ROMS 4D-Var system was applied to the 5 km resolution GOM model to hindcast the coastal hydrography and circulation in spring and summer 2010. Due the the lack of accurate information in initial, lateral boundary and surface forcing conditions, the forward ocean model failed to produce various important features in the GOM during 2010. By assimilating in situ observations into the model, the fidelity of the hindcast was improved.

SST error bias and RMSE were both reduced after data assimilation. Subsurface T/S was also improved in terms of both vertical structure and temporal evolution. Both suggest the effectiveness of the 4D-Var algorithm in fitting the observations. Independent hydrography from NEFSC surveys were compared with both

forward and posterior model solutions. Results showed a better fit of model posterior to the T/S profiles compared to forward run. Comparisons with coastal currents documented by NERACOOS buoys revealed hindcast skill improvement by the DA system. We do note, however, that the modeled coastal currents can be sensitive to the observational errors we chose for temperature and salinity.

Model fields from posterior solutions were used to understand the evolution of water masses during summer 2010. A depression in sea level offshore in the eastern GOM is an important feature introduced by the DA procedure. The resulting pressure gradient between the low pressure center and waters offshore of Penobscot Bay produces a strong offshore transport in May and June, thereby reducing the coastal flow in the western GOM. The decreased coastal flow was also documented by NERACOOS buoy B and ship-survey data in June 2010 [*Li et al.*, 2014a]. The along-shore coastal flow in the western GOM becomes more continuous in July when the low level center weakened (not shown).

Model posterior solutions were also used to estimate advection timescale for waters from the open boundary near the Scotian Shelf. The advection time scale for SSW to reach the JB is found to be 59 days. Our results demonstrate the importance of upstream and offshore forcing in controlling large variability in coastal circulation and water mass conditions in the gulf. Long-term measurements from the regional observing network are crucial in identifying anomalies, as well as being used in a data assimilative modeling framework to construct circulation hindcasts for those events. Future improvements include assimilating other available observations (e.g., coastal sea level data and altimetry) into this regional circulation prediction system, which can address a variety of marine environmental questions and problems, such as harmful algal blooms and marine fisheries.

References

Arango, H. G., J. C. Levin, E. N. Curchitser, B. Zhang, A. M. Moore, W. Han, A. L. Gordon, C. M. Lee, and J. B. Girton (2011), Development of a hindcast/forecast model for the Philippine Archipelago, *Oceanography*, 24(1), 58–69, doi:10.5670/oceanog.2011.04.

Aretxabaleta, A. L., D. J. McGillicuddy, K. W. Smith, J. P. Manning, and D. R. Lynch (2009), Model simulations of the Bay of Fundy Gyre: 2. Hindcasts for 2005–2007 reveal interannual variability in retentiveness, *J. Geophys. Res.*, 114, C09005, doi:10.1029/2008JC004948.

Beardsley, R. C., B. Butman, W. R. Geyer, and P. Smith (1997), Physical oceanography of the Gulf of Maine: An update, in *Proceedings of the Gulf of Maine Ecosystem Dynamics Scientific Symposium and Workshop*, pp. 39–52, Reg. Assoc. for Res. in the Gulf of Maine, Hanover, N. H.

Bigelow, H. B. (1927), Physical oceanography of the Gulf of Maine, *Fish. Bull.*, 40, 511–1027.

Brooks, D. A. (1994), A model study of the buoyancy-driven circulation in the Gulf of Maine, *J. Phys. Oceanogr.*, 24(11), 2387–2412.

Broquet, G., A. M. Moore, H. G. Arango, C. A. Edwards, and B. S. Powell (2009b), Ocean state and surface forcing correction using the ROMS-IS4DVAR data assimilation system, *Mercator Ocean Q. Newsl.*, 34, 5–13.

Brown, W., and J. Irish (1992), The annual evolution of geostrophic flow in the Gulf of Maine: 1986–1987, *J. Phys. Oceanogr.*, 22, 445–473.

Chapman, D. C., and R. C. Beardsley (1989), On the origin of shelf water in the Middle Atlantic Bight, *J. Phys. Oceanogr.*, 19, 384–391.

Chen, K., and R. He (2014), Mean circulation in the coastal ocean off northeastern North America from a regional-scale ocean model, *Ocean Sci. Discuss.*, 11, 2755–2790, doi:10.5194/osd-11-2755-2014.

Chen, K., R. He, B. Powell, G. Gawarkiewicz, A. M. Moore, and H. G. Arango (2014), Data assimilative modeling investigation on Gulf Stream Warm Core Ring interaction with continental shelf and slope circulation, *J. Geophys. Res. Oceans*, 119, 5968–5991, doi:10.1002/2014JC009898.

Courtier, P. (1997), Dual formulation of four-dimensional variational assimilation, *Q. J. R. Meteorol. Soc.*, 123, 2449–2461.

Curry, R. (2003), HydroBase 2.0: A database of hydrographic profiles and tools for climatological analysis, technical report, 80 pp., Woods Hole Oceanogr. Inst., Woods Hole, Mass.

Derber, J., and A. Rosati (1989), A global oceanic data assimilation system, *J. Phys. Oceanogr.*, 19, 1333–1347.

Di Lorenzo, E., A. M. Moore, H. G. Arango, B. D. Cornuelle, A. J. Miller, B. S. Powell, B. S. Chua, and A. F. Bennett (2007), Weak and strong constraint data assimilation in the inverse Regional Ocean Modeling System (ROMS): Development and application for a baroclinic coastal upwelling system, *Ocean Modell.*, 16, 160–187.

Fairall, C. W., E. F. Bradley, D. P. Rogers, J. B. Edson, and G. S. Young (1996), Bulk parameterization of air-sea fluxes for tropical ocean–global atmosphere coupled ocean-atmosphere response experiment, *J. Geophys. Res.*, 101, 3747–3764.

Fairall, C. W., E. F. Bradley, J. E. Hare, A. A. Garchev, and J. Edson (2003), Bulk parameterization of air-sea fluxes: Updates and verification for the COARE algorithm, *J. Clim.*, 16, 571–591.

Fisher, M. (1998), Minimization algorithms for variational data assimilation. Recent Developments in Numerical Methods for Atmospheric Modelling, 364–385.

Flather, R. A. (1976), A tidal model of the northwest European continental shelf, *Mem. Soc. R. Sci. Liege*, 6, 141–164.

Haidvogel, D. B., et al. (2008), Ocean forecasting in terrain-following coordinates: Formulation and skill assessment of the Regional Ocean Modeling System, *J. Comput. Phys.*, 227, 3595–3624.

He, R., D. J. McGillicuddy, B. A. Keafer, and D. M. Anderson (2008), Historic 2005 toxic bloom of Alexandrium fundyense in the western Gulf of Maine: 2. Coupled biophysical numerical modeling, *J. Geophys. Res.*, (1978–2012), 113(C7).

He, R., and R. H. Weisberg (2002), West Florida shelf circulation and heat budget for 1999 spring transition, *Cont. Shelf Res.*, 22(5), 719–748.

He, R., and R. H. Weisberg, (2003), West Florida shelf circulation and temperature budget for the 1998 fall transition, *Cont. Shelf Res.*, 23(8), 777–800.

He, R., D. J. McGillicuddy, K. W. Smith, D. R. Lynch, C. A. Stock, and J. P. Manning (2005), Data assimilative hindcast of the Gulf of Maine coastal circulation, *J. Geophys. Res.*, 110, C10011, doi:10.1029/2004JC002807.

Hetland, R. D., and R. P. Signell (2005), Modeling coastal current transport in the Gulf of Maine, *Deep Sea Res., Part II*, 52, 2430–2449.

Ingleby, B., and M. Huddleston (2007), Quality control of coean temperature and salinity profiles - historical and real-time data, *J. Mar. Syst.*, 65, 158–175.

Keafer B. A., J. H. Churchill, D. J. McGillicuddy, and D. M. Anderson (2005), Bloom development and transport of toxic Alexandrium fundyense population within a coastal plume in the Gulf of Maine, *Deep Sea Res., Part II*, 52, 2674–2697.

Kurapov, A. L., D. Foley, P. T. Strub, G. D. Egbert, and J. S. Allen (2011), Variational assimilation of satellite observations in a coastal ocean model off Oregon, *J. Geophys. Res.*, 116, C05006, doi:10.1029/2010JC006909.

Li, Y., R. He, D. J. McGllicuddy, D. M. Anderson, and B. A. Keafer (2009), Investigation of the 2006 *Alexandrium fundyense* bloom in the Gulf of Maine: In situ observations and numerical modeling, *Cont. Shelf Res.*, 29(17), 2069–2082.

Li, Y., R. He, and D. J. McGillicuddy (2014a), Seasonal and interannual variability in Gulf of Maine hydrodynamics: 2002–2011, *Deep Sea Res., Part II*, 103, 210–222.

Li, Y., R. He, and J. P. Manning (2014b), Coastal connectivity in the Gulf of Maine in spring and summer of 2004–2009, *Deep Sea Res., Part II*, 103, 199–209.

Luettich, R. A., J. J. Westerink, and N. W. Scheffner (1992), ADCIRC: An Advanced Three-Dimensional Circulation Model for Shelves, Coasts, and Estuaries. Report 1. Theory and Methodology of ADCIRC-2DDI and ADCIRC-3DL (No. CERC-TR-DRP-92-6). Coastal Engineering Research Center, Vicksburg, Miss.

Lynch, D. R., and C. G. Hannah (2001), Inverse model for limited-area hindcasts on the continental shelf, *J. Atmos. Oceanic Technol.*, 18, 962–981.

Lynch, D. R., J. T. Ipa, C. E. Naimie and F. E. Wernerb (1996), Comprehensive coastal circulation model with application to the Gulf of Maine, *Cont. Shelf Res.*, 16-7, 875–906.

Lynch, D. R., M. J. Holboke, and C. E. Naimie (1997), The Maine coastal current: Spring climatological circulation, *Cont. Shelf Res.*, 17(6), 605–634.

Lynch, D. R., C. E. Naimie, and C. G. Hannah (1998), Hindcasting the Georges Bank circulation, Part I: Detiding, *Cont. Shelf Res.*, 18, 607–639.

Marchesiello, P., J. C. McWilliams, and A. F. Shchepetkin (2001), Open boundary conditions for long-term integration of regional oceanic models, *Ocean Modell.*, 3, 1–20.

Matthews, D., B. S. Powell, and I. Janekovic (2012), Analysis of four-dimensional variational state estimation of the Hawaiian Waters, *J. Geophys. Res.*, 117, C03013, doi:10.1029/2011JC007575.

McGillicuddy, D. J., D. W. Townsend, R. He, B. A. Keafer, J. L. Kleindinst, Y. Li, J. P. Manning, D. G. Mountain, M. A. Thomas, and D. M. Anderson (2011), Suppression of the 2010 Alexandrium fundyense bloom by changes in physical, biological, and chemical properties of the Gulf of Maine. *Limnol. Oceanogr. Methods*, 56(6), 2411–2426.

Mellor, L. G., and T. Yamada (1982), Development of a turbulence closure model for geophysical fluid problems, *Rev. Geophys.*, 20, 851–875.

Moore, A. M., H. G. Arango, E. D. Lorenzo, B. D. Cornuelle, A. J. Miller, and D. J. Neilson (2004), A comprehensive ocean prediction and analysis system based on the tangent linear and adjoint of a regional ocean model, *Ocean Modell.*, 7, 227–258.

Moore, A. M., H. G. Arango, G. Broquet, C. Edwards, M. Veneziani, B. Powell, D. Foley, J. D. Doyle, D. Costa, and P. Robinson (2011a), The Regional Ocean Modeling System (ROMS) 4-Dimensional Variational Data Assimilation Systems: Part2—Performance and application to the California Current System, *Prog. Oceanogr.*, 91, 50–73.

Moore, A. M., H. G. Arango, G. Broquet, B. Powell, A. T. Weaver, and J. Zavala-Garay (2011b): The Regional Ocean Modeling System (ROMS) 4-Dimensional Variational Data Assimilation Systems: Part1—System overview and formulation, *Prog. Oceanogr.*, 91, 34–49.

Pettigrew, N. R., R. J. Fleming, and C. P. Fikes (2011), The history of the first decade of the observing system in the Gulf of Maine, and plans for the second decade, *MTS J.*, 1–10.

Powell, B. S., H. Arango, A. M. Moore, E. D. Lorzenzo, R. F. Milliff, and D. Foley (2008), 4DVAR Data Assimilation in the Intra-Americas Sea with the Regional Ocean Modeling System (ROMS), *Ocean Modell.*, 25, 173–188.

Powell, B. S., and A. M. Moore (2009), Estimating the 4DVAR analysis error of GODAE products, *Ocean Dynam.*, 59(1), 121–138.

Shcheptkin, A. F., and J. C. McWilliams (2005), A split-explicit, free-surface, topographic following-coordinate oceanic model, *Ocean Modell.*, 9, 347–404.

Signell, R. P., H. L. Jenter, and A. F. Blumberg (1994), Modeling the seasonal circulation in Massachusetts Bay, in *Proceedings of 3rd International Conference on Estuarine and Coastal Modeling*, edited by M. L. Spaulding, pp. 578–590, Am. Soc. of Civ. Eng., Reston, Va.

Smith, P. C. (1983), The mean and seasonal circulation off southeast Nova Scotia, *J. Phys. Oceanogr.*, 13, 1034–1054.

Smith, P. C., R. W. Houghton, R. G. Fairbanks., and D. G. Mountain (2001), Interannual variability of boundary fluxes and water mass properties in the Gulf of Maine and on Georges Bank: 1993–1997, *Deep Sea Res., Part II*, 48, 37–70.

Smith, P. C., N. R. Pettigrew, P. Yeats, D. W. Townsend, and G. Han (2012), Regime shift in the Gulf of Maine, in *Advancing an Ecosystem Approach in the Gulf of Maine*, edited by R. L. Stephenson, pp.185–203, Am. Fish. Soc., Bethesda, Md.

Townsend, D. W., N. D. Rebuck, M. A. Thomas, L. Karp-Boss, and R. M. Gettings (2010), A changing nutrient regime in the Gulf of Maine, *Cont. Shelf Res.*, 30, 820–832.

Weaver, A. T., and P. Courtier (2001), Correlation modelling on the sphere using a generalized diffusion equation, *Q. J. R. Meteorol. Soc.*, 127, 1815–1846.

Weaver, A. T., J. Vialard, and D. L. T. Anderson (2003), Three- and four-dimensional variational data assimilation with a general circulation model of the tropical Pacific Ocean. Part1: Formulation, internal diagnostics, and consistency checks, *Mon. Weather Rev.*, 131, 1360–1378.

Xue H., F. Chai, and N. R. Pettigrew (2000), A model study of the seasonal circulation in the Gulf of Maine, *J. Phys. Oceanogr.*, 30(5), 1111–1135.

Zavala-Garay, J., J. L. Wilkin, and H. G. Arango (2012), Predictability of mesoscale variability in the East Australian Current given strong-constraint data assimilation, *J. Phys. Oceanogr.*, 42, 1402–1420.